Article:
Asiagbe, KS, Colombo, M, Fairweather, M et al. (2020) Computational modelling of microbubble coalescence and breakup using large eddy simulation and Lagrangian tracking. AIChE Journal, 66 (11). e17017. ISSN: 0001-1541

https://doi.org/10.1002/aic.17017

Computational modelling of microbubble coalescence and breakup using large eddy simulation and Lagrangian tracking

Kenneth S. Asiagbe, Marco Colombo, Michael Fairweather and Derrick O. Njobuenwu
School of Chemical and Process Engineering, University of Leeds, Leeds LS2 9JT, UK

Abstract
The flow of dispersed microbubbles was studied with an Eulerian-Lagrangian technique using large eddy simulation to predict the continuous liquid flow and Lagrangian tracking to compute bubble trajectories. The model fully accounts for bubble coalescence and breakup and was applied to horizontal and vertical channel flows. With low levels of turbulence, gravity in horizontal, and lift in vertical, channel flows govern the bubble spatial and collision distribution. When turbulence is sufficiently high to, at least partially, oppose bubble preferential concentration, more uniform collision and coalescence distributions are found, although these remain peaked near the wall in both configurations. Almost 100% coalescence efficiency was always found, due to bubbles colliding along similar trajectories, with breakup only recorded in a flow of low surface tension refrigerant R134a. Models like this can provide the required quantitative understanding of the microbubbles complex behaviour, as well as supporting the development of more macroscopic modelling closures.

Keywords
Eulerian-Lagrangian, large eddy simulation, microbubbles, bubble coalescence, breakup.

Introduction
In multiphase flows, the flow pattern is termed ‘dispersed’ when one of the phases develops into an almost continuous background with small discrete entities of one or more additional phases dispersed within it. When gas bubbles are dispersed in a liquid phase, the flows is commonly referred to as a bubbly flow[1]. Bubbly flows are relevant in a large variety of industrial sectors and technological applications, including thermal power generation and nuclear power plants, chemical and petrochemical reactors, oil and gas extraction and

transportation, bioenergy, aeration and waste water treatment equipment, and medical and biomedical procedures, to name but a few.

In most of these applications, the bubbles' role is usually to increase the heat (in boiling) and mass and momentum transfer rates within the flow by interacting with and promoting the mixing of the continuous fluid phase[2,3]. Fluid flow affects the bubble position and concentration patterns, and the bubbles alter the mean and turbulent fluid motion[4-6]. These mutual interactions greatly complicate the analysis of bubbly flows and make the accurate prediction of their thermo-fluid dynamics particularly challenging. In addition, interfacial heat and mass transfer rates are driven by the interfacial area density and the bubble size distribution in the flow[7,8]. These are in continuous evolution as a consequence of bubble-bubble interactions that promote bubble coalescence, and bubble-fluid interactions that can induce bubble breakup[9,10]. In view of all these complexities, bubbly flows have been the subject of numerous experimental and numerical efforts aimed at improving our understanding and modelling capabilities, which are still far from comprehensive and satisfactory[11-19].

In the literature, most studies have focused on bubbles with diameters of a few millimetres, driven by the relevance of the bubbly flow regime during boiling and the role of bubble mixing in chemical, petrochemical and process engineering equipment such as bubble columns. However, more recently, attention has shifted to much smaller bubbles, having diameters of micro or even nanometers[20-23]. Microbubbles are increasingly used in innovative applications such as the targeted delivery of drugs and anti-tumour medicines in the human body[24,25]. Other major interests are in relation to the aeration and treatment of waste water[26,27], and the reduction of drag on immersed bodies by the release of microbubbles near the solid surface[22,28]. In view

of this, it is critical to increase knowledge and the modelling tools available to predict the detailed behaviour of these microbubbles and their interaction with the background fluid phase. In recent years, computational fluid dynamics, with its ability to account for local, small-scale physical effects on the large-scale fluid motion, has become increasingly popular for the prediction of the complex hydrodynamics of multiphase flows. Many different methods have been applied to the prediction of bubbly flows. At the industrial scale, multi-fluid Eulerian-Eulerian models, where interface transfers are entirely modelled, are still the preferred choice because of the relatively limited computational effort required in their solution[11,14,15,29]. On the other hand, interface tracking techniques that fully-resolve the bubble-fluid interface, coupled with direct numerical simulation (DNS) of the background fluid phase flow, have now reached maturity. Although still limited to fundamental studies of a relatively small number of bubbles, these models are driving physical understanding of the complex and small-scale physics of bubbly flows[4,30-32].

Because of their small size, microbubbles have also been successfully modelled with Eulerian-Lagrangian techniques, where bubble trajectories are deterministically tracked through the background Eulerian phase by solving an equation of motion for each individual bubble. Giusti et al.[21] studied the one-way coupled flow of microbubbles and their distribution induced by interactions with the main fluid motion in a vertical channel upflow. In their Eulerian-Lagrangian model, the fluid phase was resolved using DNS. Later, Molin et al.[22] extended the capability of the DNS Eulerian-Lagrangian method to a two-way coupled flow, where feedback effects from the bubbles to the fluid flow are also accounted for. These authors studied the distribution of bubbles in upflow and downflow channels, and the modifications induced by the bubbles on the fluid mean and turbulent motion. Pang et al.[33] also applied an Eulerian-Lagrangian model, with the fluid phase resolved by DNS, to horizontal one-way and two-way

coupled flows in order to study drag reduction on the walls of a channel. Kuipers and co-workers[34,35] extended the applicability of these techniques to bubbles of a few millimetres diameter in large-scale recirculation systems such as bubble columns. The studies noted have greatly assisted the detailed understanding of the behaviour of microbubbles in turbulent flows and their mutual interactions with the fluid phase.

In this work, a Lagrangian bubble tracker is coupled with large eddy simulation (LES) of the fluid phase. LES allows resolution of most of the relevant scales of turbulent fluid motion responsible for influencing the bubble motion. At the same time, the reduced computational effort that results from modelling, rather than simulating, the small-scale turbulent fluctuations makes it possible to extend the methods' applicability to turbulent flows closer to conditions that are of industrial interest. In previous works, we have applied a similar approach to two-way coupled horizontal[36], and upward and downward vertical, channel flows[20], addressing the interactions between the fluid and the microbubbles, and feedback of the bubbles to the turbulence in the fluid phase. In this work, the model is extended to four-way coupled flows (two-way coupled plus bubble collision, coalescence and breakup) by accounting for interactions between the bubbles, and bubble coalescence and breakup. Horizontal and vertical channel flows are addressed and the conditions that promote or impede coalescence are analysed, as is the spatial distribution of coalescence events across the channels. The effects of turbulence on collision and coalescence patterns are also analysed. The results provide a quantitative assessment of the impact of coalescence and breakup events on microbubble behaviour, as well as some of the much required additional physical understanding of bubble coalescence and breakup that can be used to underpin the development of better macroscopic modelling closures. In this context, results from highly-resolved simulations are increasingly

being used to improve the interfacial closures implemented in multi-fluid Eulerian-Eulerian models [37,38].

Numerical Modelling

Large eddy simulation

The LES for the fluid phase flow solves filtered continuity and momentum balance equations for an incompressible fluid:

$$\frac{\partial \bar{u}_i}{\partial x_i} = 0 \tag{1}$$

$$\frac{\partial \bar{u}_i}{\partial t} + \bar{u}_j \frac{\partial \bar{u}_i}{\partial x_j} = -\frac{1}{\rho_l}\frac{\partial \bar{p}}{\partial x_i} - \frac{\partial}{\partial x_j}\left(\bar{\sigma}_{ij} + \tau_{ij}\right) + \frac{\overline{\Delta p}}{\rho_l L_z}\delta_{i3} + \frac{f_{2w}}{\rho_l} \tag{2}$$

Filtered variables are identified with an overbar, ρ_l is the fluid density, u is the fluid velocity and p is the pressure. The penultimate term on the right hand side (RHS) of Eq. (2) represents the mean pressure gradient that drives the flow. In the vertical channel, a term that accounts for the change in density of the mixture after bubble injection is also included in order to maintain a constant total pressure drop:

$$\frac{\overline{\Delta p}}{L_z} = -\frac{\rho_l u_\tau^2}{h} \pm \alpha_b(\rho_l - \rho_b)g \tag{3}$$

where u_τ is the fluid shear velocity, h the channel half-height, ρ_b and α_b the bubble density and volume fraction, and g the gravitational acceleration. The ± sign depends on the orientation of the channel. The last term on the RHS of Eq. (2) accounts for two-way coupling feedback per unit volume of the bubbles on the fluid, f_{2w}, obtained from the summation of all the hydrodynamic forces acting on the bubbles:

$$f_{2w} = \frac{1}{\Delta^3}\sum_{j=1}^{n_b} f_{H,j} \tag{4}$$

In Eq. (4), the summation is over the number of bubbles n_b in each finite-volume cell, with $f_{H,j}$ being the source term for the j^{th} bubble and H the sum of all the hydrodynamic forces (drag,

shear-lift, pressure gradient and added mass). Body forces were included in the pressure gradient term (Eq. (3)). In Eq. (2), $\bar{\sigma}_{ij}$ is the viscous stress tensor:

$$\bar{\sigma}_{ij} = -2\nu_l \bar{S}_{ij} = -\nu_l \left(\frac{\partial \bar{u}_i}{\partial x_j} + \frac{\partial \bar{u}_j}{\partial x_i} \right) \tag{5}$$

where ν_l is the fluid kinematic viscosity and S_{ij} the filtered strain-rate tensor. Finally, τ_{ij} is the sub-grid scale (SGS) stress tensor arising from the filtering operation:

$$\tau_{ij} = \overline{u_i u_j} - \bar{u}_i \bar{u}_j \tag{6}$$

This term is closed with the product of an SGS turbulent kinematic viscosity ν_{sgs} and the resolved part of the strain-rate tensor. The SGS kinematic viscosity is calculated from the dynamic Smagorinsky model[39,40] as the product of the filter width Δ and an appropriate velocity scale:

$$\nu_{sgs} = (C\bar{\Delta})^2 \|\bar{S}\| \tag{7}$$

where $||\bar{S}|| = \sqrt{2\bar{S}_{ij}\bar{S}_{ij}}$. The model coefficient C is dynamically determined by applying a second test filter operation:

$$T_{ij} = \widetilde{\overline{u_i u_j}} - \tilde{\bar{u}}_i \tilde{\bar{u}}_j \tag{8}$$

To derive the required expression for C, some form of relationship between the model constant values C^2 and $\tilde{C}^2$ at the grid- and test-filter levels must be specified. Based on the hypothesis that the cut-off length falls inside the inertial sub-range, $C^2 = \tilde{C}^2$ is the generally used approximation. However, this is not guaranteed to occur in wall bounded or low Reynolds number flows and the two model parameters are liable to differ, particularly in the region of weakest resolved strain. To account for this, di Mare and Jones[41] proposed the following:

$$\tilde{C}^2 = C^2 \left(1 + \frac{\varepsilon}{2\sqrt{2\widetilde{\Delta}^2} \, \| \, \tilde{\bar{s}} \, \| \| \, \tilde{\bar{s}}^a \, \|^2} \right) \tag{9}$$

where $\varepsilon \approx v^3 / l$ is the assumed turbulence energy dissipation rate, v and l a velocity and length scale, and s^a is the anisotropic part of the strain rate tensor. In Eq. (9), if the cut-off falls inside the inertial sub-range, the modelled dissipation represents the entire dissipation in the flow. Conversely, in the high Reynolds number limit, the ratio of ε to the test filter width and test-filtered strain rate measures how far the flow is from scale preserving conditions. The coefficient C^2 is then obtained from:

$$C^2 = \frac{\left[2\sqrt{2(C_*^2\Delta)^2} \parallel \tilde{\bar{s}} \parallel \parallel \tilde{\bar{s}}_{ij}^a \parallel \tilde{\bar{s}}_{ij}^a - L_{ij}^a \tilde{\bar{s}}_{ij}^a\right]}{\varepsilon + 2\sqrt{2\widetilde{\bar{\Delta}}^2} \parallel \tilde{\bar{s}} \parallel \parallel \tilde{\bar{s}}^a \parallel^2} \tag{10}$$

where C_*^2 is a provisional value for C^2, taken as its value at the previous time step[40]. The parameter L_{ij}, known as Germano's identity (Germano et al.[39]), relates the test-filtered and grid-filtered stress tensors, both of which are known (i.e. resolved) quantities. Overall, the above method is well-conditioned and avoids possible irregular behaviours sometime exhibited by other implementations. When the resolved strain tends to zero, C^2 also tends to zero, while $\tilde{C}^2$ remains bounded. The dissipation term yields smooth C^2 values without a need for averaging, and the maxima of C^2 are of the same order of magnitude as Lilly's[42] estimate for the Smagorinsky model constant. Negative values of the model parameters are not prevented and in such circumstances, the value of the model constant, and the SGS viscosity, are set to zero to prevent model instability. A box filter is used with $\bar{\Delta} = \left(\Delta_x \Delta_y \Delta_z\right)^{1/3}$, where Δ_x, Δ_y and Δ_z denote the physical grid spacing in the three coordinate directions. The ratio of the test to the grid filter was set to 2.

Lagrangian tracking of bubble motion

Bubble motion in the turbulent flow field is obtained by solving Newton's second law for each individual bubble[43], written per unit mass:

$$\frac{d\boldsymbol{v}}{dt} = \left(1 - \frac{\rho_l}{\rho_b}\right) g + \frac{\boldsymbol{u} - \boldsymbol{v}}{\tau_b} C_D + C_L \frac{\rho_l}{\rho_b} [(\boldsymbol{u} - \boldsymbol{v}) \times \boldsymbol{\omega}] + \frac{\rho_l}{\rho_b} \frac{d\boldsymbol{u}}{dt} + \frac{\rho_l}{2\rho_b} \left(\frac{d\boldsymbol{u}}{dt} - \frac{d\boldsymbol{v}}{dt}\right) + \boldsymbol{\chi_{sgs}}. \quad (11)$$

The velocity of the microbubble is $\boldsymbol{v}$ and the microbubbles are subjected to gravity and buoyancy, drag, lift, pressure gradient and added mass forces while the Basset history force, being demonstrated negligible in comparison to the other forces, has been neglected[44,45]. The last term on the RHS is a stochastic contribution from the unresolved SGS velocity fluctuations. The bubble relaxation time τ_b is corrected to account for added mass effects, giving $\check{\tau}_b = \tau_b(1 + \rho_l/2\rho_b)$, and $\boldsymbol{\omega}$ is the fluid vorticity. The bubble position vector $\boldsymbol{x_b}$ is obtained by further differentiation of Eq. (11).

The drag coefficient C_D is function of the bubble Reynolds number ($Re_b = |\boldsymbol{u} - \boldsymbol{v}|\, d_b / \nu$)[46]:

$$C_D = (1 + 0.15 Re_b^{0.687}) \quad (12)$$

The above model is sufficient for the bubbles considered in this work, which have diameters of fractions of a millimetre which will maintain an almost spherical shape. Implementation of additional models, specifically developed for bubbles[47,48], will be pursued in future works when a larger range of bubble sizes is considered. The lift coefficient C_L is computed from the correlation of Legendre and Magnaudet[49]. The contribution from the unresolved SGS fluctuations is determined using a stochastic Markov model[50]:

$$\boldsymbol{\chi_{sgs}} = C_0 \left(\frac{k_{sgs}}{\tau_t}\right) d\boldsymbol{W}_t / \mathrm{d}t \quad (13)$$

where k_{sgs} is the unresolved kinetic energy of the liquid phase, calculated from equilibrium arguments[50], and C_0 is a model constant taken as unity. $d\boldsymbol{W_t}$ is the increment of the Wiener process, obtained from a random variable sampled from a normal distribution of zero mean and unity variance and the solver time step. The sub-grid timescale τ_t is related to the rate of interaction between the bubble and turbulence dynamics according to:

$$\tau_t = \frac{\tau_b^{1.6}}{\left(\Delta / k_{sgs}^{0.5}\right)^{0.6}} \tag{14}$$

Four-way coupling

When the concentration of bubbles becomes significant, not only their feedback to the liquid phase but also the interactions between them are no longer negligible. To properly accommodate such conditions, the model has been extended to a four-way coupled approach, by adding bubble collision, coalescence and breakup to the two-way coupled model.

Only binary collisions are considered and these are treated with the hard-sphere collision approach. In addition, collision is likely to occur only between neighbouring bubbles, separated by a relative distance sufficiently small to be covered during the small time step employed in the computation. Therefore, saving of significant computational time without loss of accuracy is obtained by limiting the collision detection for each bubble to neighbours under a certain relative distance. To achieve this, the computational domain is split into virtual cells, the size of which can be dynamically adjusted during the simulation, and collision is only checked between bubbles inside the same cell[51,52]. After this first search, a second detection step is performed by employing slightly larger virtual cells to account for potential collisions between bubbles located near the cell borders. The ratio between the second and the first cell dimensions was taken equal to 1.3, as suggested by Breuer and Alletto[53].

In each computational cell, assuming the bubble velocity remains constant during each time step, a first check is successful if the product of the two bubbles' relative distance and velocity is negative, given that to collide the bubbles must approach one another. A second check is then made to ensure that the minimum distance between the bubbles during the time step is less than the sum of their radii:

$$\boldsymbol{x}_{r,min} = \boldsymbol{x}_r + \boldsymbol{v}_r \, \Delta t_{min} \tag{15}$$

The minimum time Δt_{min} is the interval after which the bubbles are at their minimum distance:

$$\Delta t_{min} = -\frac{\boldsymbol{x}_r \boldsymbol{v}_r}{|\boldsymbol{v}_r|^2} \tag{16}$$

If the minimum time is less than or equal to the time step, and the minimum distance less than the sum of the radii of the colliding bubbles, a collision occurs and the time interval for collision Δt_{coll} is calculated as the time required for the distance between the bubbles to equal to sum of their radii r_{12}:

$$\left|\boldsymbol{x}_{r,coll}\right| = \left|\boldsymbol{x}_r + \boldsymbol{v}_{b,r}\, \Delta t_{coll}\right| = r_{12} \tag{17}$$

Once a collision is detected, the occurrence of coalescence is evaluated using the film drainage model[54]. The model assumes that when two bubbles approach one another, a thin liquid film that prevents immediate coalescence is trapped between the bubble surfaces. Coalescence only occurs if the contact time between the bubbles is long enough to allow drainage of the liquid film to a thickness small enough for rupture of the film to occur. Therefore, the constraint for coalescence in the model is the contact time being larger than the drainage time. The contact time is modelled using the approach of Sommerfeld et al.[55]:

$$\tau_{ij} = \frac{0.25 \cdot R_{ij}}{v_n} \tag{18}$$

In the previous equation, R_{ij} is the equivalent bubble radius $2 \cdot (2 \,/\, d_{b1} + 2 \,/\, d_{b2})^{-1}$ and v_n the relative approach velocity in the normal direction. For the drainage time, different options are available and a good overview is provided in Liao et al[10]. Here, although derived a few years ago, the film drainage time is taken directly from Prince and Blanch[54]:

$$t_{ij} = \sqrt{\frac{R_{ij}^3 \rho_l}{16\sigma}} \ln\left(\frac{h_i}{h_f}\right) \tag{19}$$

The initial and final film thickness h_i and h_o are taken equal to 10^{-4} and 10^{-8}, respectively[54]. After collision, the volume of the new bubble is set equal to the sum of the volumes of the

colliding bubbles. The position and initial velocity of the coalesced bubble are obtained from the mass-weighted average of those of the colliding bubbles. When the contact time is lower than the film drainage time, the two bubble bounce off one another without coalescing and the new bubble velocities are obtained from momentum conservation for a hard-sphere collision.

In a turbulent flow, bubbles can also breakup because of pressure fluctuations induced on the bubble surface by the turbulent stresses. For breakup to occur, the stresses induced by turbulence need to overcome the surface tension forces that tend to restore the bubble shape. The model employed is taken from Martinez-Bazan et al.[56] and adapted to the Eulerian-Lagrangian framework. The surface restoring force, derived from the minimum energy required to deform a bubble of size d_b, equals:

$$\tau_s = 6\frac{\sigma}{d_b} \tag{20}$$

The turbulence induced stress is proportional to the velocity difference over a distance equal to the bubble diameter d_b. Assuming the bubble is in the inertial subrange, this can be modelled as:

$$\tau_t(d_b) = \frac{1}{2}\rho_l \beta \varepsilon^{2/3} d_b^{2/3} \tag{21}$$

where the constant β = 8.2 and ε is the turbulence energy dissipation rate. The previous expressions can be rearranged into a breakup criterion, expressed as a function of a critical Weber number:

$$We_{crit} = \frac{\rho_l \varepsilon^{2/3} d_b^{5/3}}{\sigma} > We_{crit} = 12 \tag{24}$$

Binary breakup is assumed and daughter bubbles after breakup have equal size and their location is initially that of the parent bubble.

Numerical framework

The computational domain is a channel, bounded by two infinite flat parallel walls, of dimensions $2h \times 2\pi h \times 4\pi h$, where h is the half-channel width. Figure 1 illustrates the horizontal and vertical configurations, where the x, y and z axes identify the wall-normal, spanwise and streamwise directions, respectively. The no-slip boundary condition was imposed at the channel walls and periodic boundary conditions were applied in the streamwise and spanwise directions. In the streamwise direction, the flow is driven by an imposed pressure gradient. In vertical channels, this also accounts for changes in the mixture density after bubble injection (Eq. (3)), essentially maintaining constant the sum of gravitational and frictional pressure losses. Therefore, the lighter mixture is allowed to flow faster in upflow while, in downflow, the flow is slower because of the reduced gravitational gain. Because of this, different values of the shear velocity u_τ and Reynolds number Re_τ are obtained with respect to the single-phase flow, and these are summarized in Table 1 for the vertical channel and the two reference single-phase shear Reynolds number flows tested, Re_τ = 150 and 590. In the water-air calculations, a density ρ_l = 1000 kg m^{-3} and kinematic viscosity $\nu = 10^{-6}$ m^{2}s^{-1} were used. To study breakup in more detail, an additional simulation for refrigerant R134a, having a much lower surface tension, at Re_τ = 1154 was made in the vertical channel. For this flow, a density ρ_l = 1206.5 kg m^{-3} and kinematic viscosity $\nu = 9.7 \cdot 10^{-7}$ m^{2}s^{-1} were employed.

The computational domain was discretized with 129 × 128 × 128 grid points. Grid nodes are distributed uniformly in the y and z axes, while a hyperbolic function[57] was used to achieve the necessary grid-refinement near the walls in the wall-normal direction. The BOFFIN (Boundary Fitted Flow Integrator) code[50] was used to solve the governing flow equations. The convective terms of the equations written in their conservative form were discretized using a second-order central difference scheme. In time, a second-order, three-point backward implicit scheme of the Gear family[58] was used. The pressure-velocity coupling was solved using a SIMPLE-type

routine[59], with a Rhie and Chow[60] pressure smoothing routine to prevent uncoupling of the pressure and velocity fields and a two-step approximate factorization, which means an approximate intermediate solution between the old time step n and the new time step $n + 1$ is calculated in the first step, before the final solution at $n + 1$. The system of algebraic equations for velocity was solved using the preconditioned bi-conjugate gradient method of Van der Vorst[61], while the conjugate gradient method with incomplete Cholesky preconditioning (ICCG[62]) was used for the pressure. For additional details, readers are referred to previous publications of LES studies of reacting[63,64] and non-reacting turbulent flows[50,65].

For the multiphase simulations, air bubbles having a density ρ_b = 1.3 kg m^{-3} were uniformly introduced into fully-converged single-phase flow solutions at the two shear Reynolds numbers considered. For the R134a flow, vapour bubbles of density ρ_b = 28.4 kg m^{-3} were used. At injection, the bubble initial velocity is assumed equal to the velocity of the fluid at the same position. In total, three bubble sizes, d_b = 110, 220 and 330 μm, were employed, and the bubble volume fraction was fixed to $\alpha_b = 10^{-3}$, high enough to observe a significant number of bubble collisions. For the channel investigated, this corresponds to 181,272 microbubbles for d_b = 110 μm, 22,700 for d_b = 220 μm and 6,714 for d_b = 330 μm. For the maximum number of bubbles employed (181,272), the number of computational cells (more than 2 million) used ensures a high resolution of the two-way coupled flow field, with only a few bubbles simultaneously present in the same cell. Therefore, no significant dependencies of the two-way coupling term on the mesh are expected. Further details of relevant liquid and bubble parameters used in the simulations are given in Table 2.

Bubble motion is obtained by integration of Eq. (11) using a fourth-order Runge-Kutta scheme. Periodic conditions are also imposed on the bubbles in the streamwise and spanwise directions.

Therefore, when a bubble crosses a boundary surface in these directions, it is re-injected in a specular position on the opposite boundary surface at the next time-step. When bubbles hit the wall, an elastic collision is assumed. Even though this is a simplistic assumption, given that bubbles may deform when approaching and hitting a wall, a reliable and robust modelling framework for such interactions is not yet available. The time-step used for the bubble tracker was chosen to be equal to the fluid flow solver time-step, this corresponding to roughly one-quarter of the bubble response time ($\tau_b = \rho_b d_b^2/18\mu$) for both Reynolds numbers considered. The total simulation time, expressed in wall units from $t^+ = tu_\tau^2/\upsilon$ (where t is the computational time in seconds), was sufficient to obtain statistically steady flow solutions, and allow the derivation of converged averaged values of fluid and bubble velocity statistics and provide sufficient data to characterize bubble coalescence and breakup behaviour. Simulation times varied from 700 t^+ for the horizontal channel to 2600 t^+ for the vertical channel at Re_τ = 590. The present work mainly focuses on the extension of the previous model to four-way coupling (two-way coupling plus bubble collision, coalescence and breakup) and associated results. Validation of the model has been previously obtained for single-phase, one-way and two-way coupled simulations in both horizontal and vertical channels[20,36].

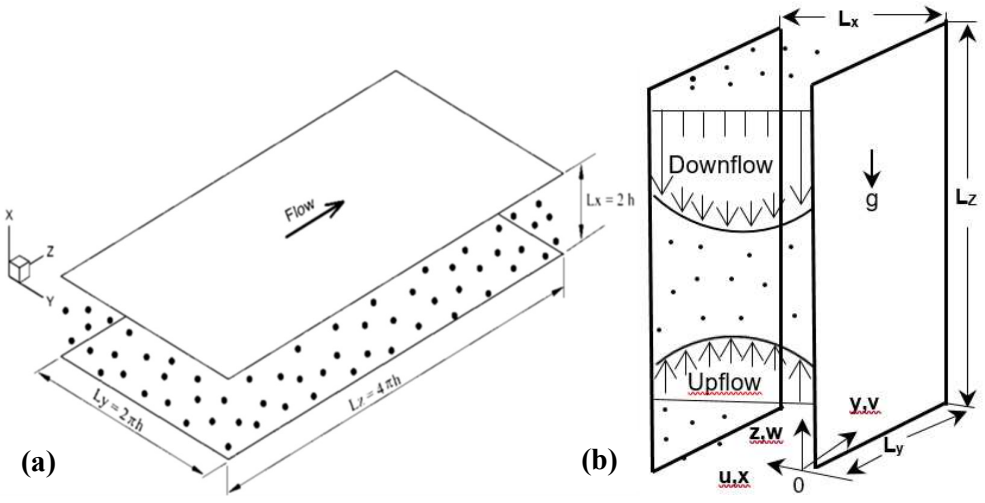

Figure 1. Coordinate system and channel geometry: (a) horizontal channel; (b) vertical channel.

Table 1: Reynolds number and shear velocity for the four-way coupled simulations in the different geometries.

	Horizontal	Vertical Upward	Vertical Downward	Vertical R134a
Re_τ [-]	150	172	122	-
u_τ [m s^{-1}]	7.5×10^{-3}	8.58×10^{-3}	6.11×10^{-3}	-
Re_τ [-]	590	612	562	1154
u_τ [m s^{-1}]	2.95×10^{-2}	3.06×10^{-2}	2.81×10^{-2}	5.6×10^{-2}

Table 2. Fluid and mixture properties and bubble parameters.

	ρ_l [kg m^{-3}]	ν_l [kg m^{-3}]	ρ_b [kg m^{-3}]	d_b [µm]	σ [N m^{-1}]
Air-Water	1000	10^{-6}	1.3	110, 220, 330	0.072
R134a	1206.5	9.7×10^{-7}	28.4	110, 220	8.08×10^{-3}

Results and discussion

Horizontal channel

The numerical model was first applied to horizontal channel flows. The same configuration was predicted and analysed in a previous publication, where validation of the numerical model was obtained for single-phase and two-way coupled simulations[36]. In this work, and starting from fully-developed single-phase flow conditions at Re_τ = 150 and 590, bubbles were injected and allowed to interact with the turbulent fluid flow and with one another. The mean streamwise fluid and bubble velocity profiles, normal turbulent stresses and the Reynolds shear stress are presented in Figure 2 for the Re_τ = 590 case. Comparable results were obtained at a shear Reynolds number of 150. Although the bubbles transport, interact, collide and coalesce, the velocity field remains in close agreement with its single-phase counterpart, given the relatively low value of the gas void fraction. The bubbles move with the fluid at an almost equal velocity and show very similar values of turbulent fluctuations. Therefore, their behaviour is mainly dictated by the continuous fluid flow in this regard.

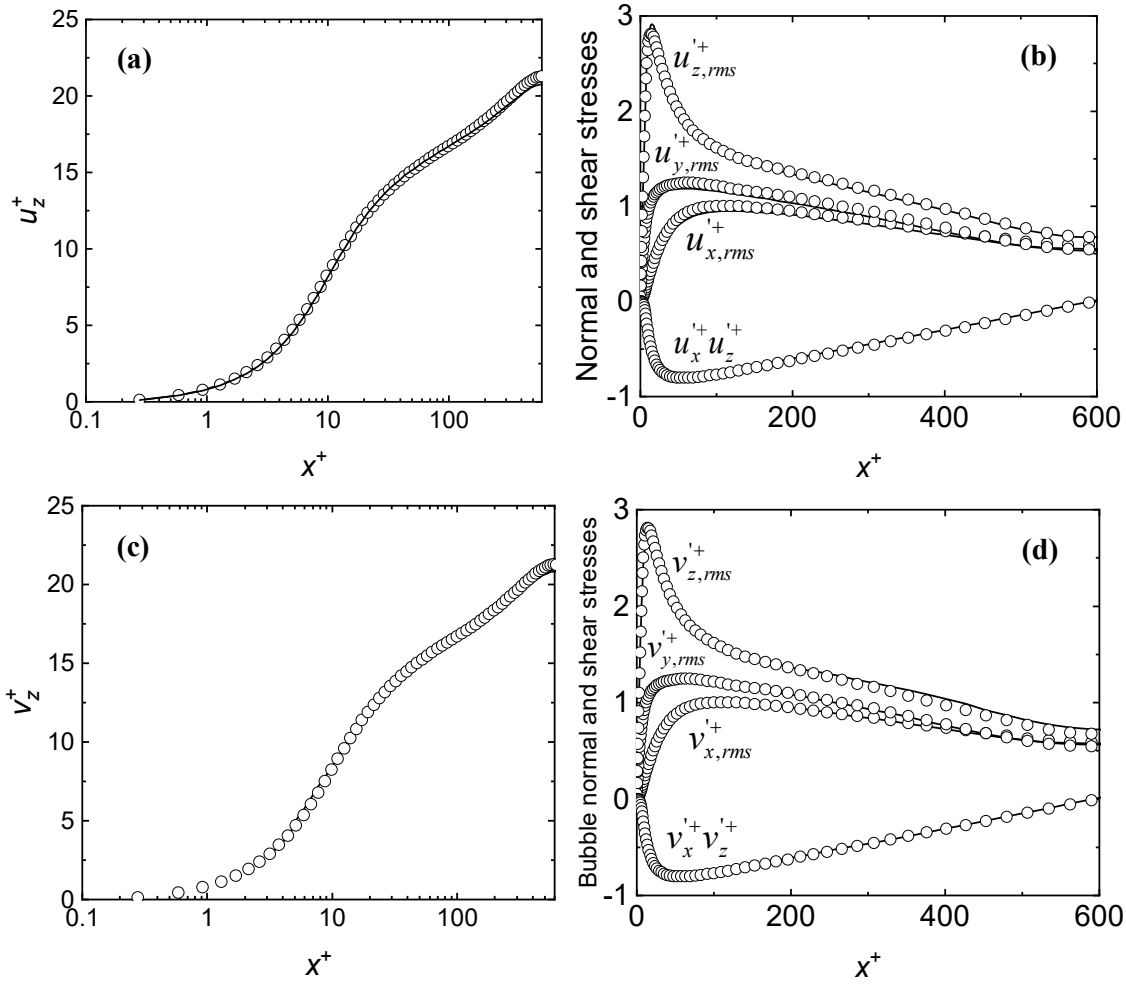

Figure 2. Wall-normal profiles in the horizontal channel at $Re_\tau = 590$: (a) mean fluid streamwise velocity; (b) fluid normal and shear turbulent stresses; (c) bubble mean streamwise velocity; (d) bubble normal and shear turbulent stresses (○ single-phase; ─ four-way coupled).

The buoyant nature of the gas bubbles is, however, evident in the bubble concentration profiles given in Figure 3. At the beginning of the simulations, the bubbles have a uniform distribution. However, as soon as the simulations start, they are driven towards the upper regions of the channel due to their lower density, and accumulate at the upper wall. In Figure 3, the results at both 150 and 590 shear Reynolds numbers are provided and the effect of the turbulence on the bubble distribution is evident. Overall, random turbulent motion tends to disperse the bubbles and opposes gradients in their concentration. At $Re_\tau = 150$, the turbulence is rather weak and in a short time almost no bubbles are found in the lower half of the channel. At $Re_\tau = 590$, in contrast, the higher turbulence levels impact the bubble distribution more significantly.

Although the peak at the upper wall remains, therefore, bubbles are still present in the lower section of the channel and their migration towards the upper regions is much slower.

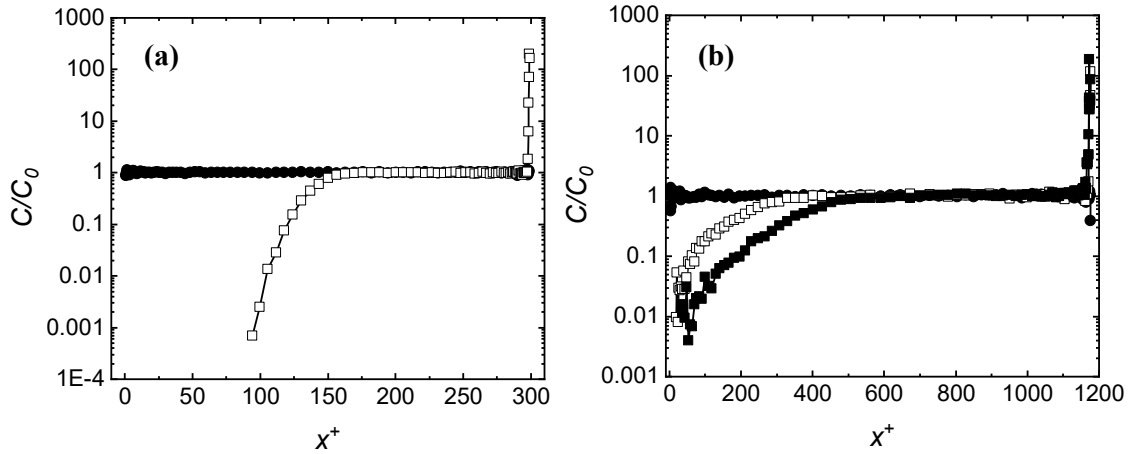

Figure 3. Microbubble normalised wall-normal concentration profiles in the horizontal channel flows at: (a) Re_τ = 150 (● t^+ = 0; □ t^+ = 50 – 100); (b) Re_τ = 590 (● t^+ = 0; □ t^+ = 300 – 500; ■ t^+ = 500 – 700).

The spatial distribution in the wall-normal direction of the collision and coalescence events is provided in Figure 4(a) and (b) at Re_τ = 150 and 590, respectively, and the corresponding time evolution in the two flows of bubbles of different sizes is given in Figure 4(c) and (d). In the latter plots, the numbers identify how many bubbles have coalesced, so that 1 identifies bubbles of original size of 220 μm, 2 bubbles formed by the coalescence of two bubbles and so on. Also, in these and following plots, *n* on the ordinate identifies the number of collisions and coalescences (Figure 4(a) and (b)) or the number of bubbles of a certain size (Figure 4(c) and (d)) normalized by the initial number of bubbles injected. Although the higher level of turbulence in the Re_τ = 590 flow should promote bubble collision, the total number of collisions is actually higher in the Re_τ = 150 flow because of the much larger concentration of bubbles in the upper regions of the channel. This is clear from the number of collisions and coalescences shown in Figure 4(a) and (b). At Re_τ = 150, collisions and coalescences are largely concentrated in the very near-wall region (Figure 4(a)). Conversely, away from the wall, both are higher at Re_τ = 590 (Figure 4(b)).

From the results of Figure 4, it is also evident how the large majority of collisions result in the coalescence of the bubbles. The occurrence of coalescence is modelled based on film drainage theory and, for coalescence to occur, the contact time between the bubbles needs to be greater than the film drainage time. The contact time is inversely proportional to differences in the velocity and direction between colliding bubbles (Eq. (18)). When bubbles move in different directions and with significantly different velocities, therefore, their contact time is small. Therefore, even at $Re_\tau = 590$, bubble trajectories are still significantly influenced by the fluid mean motion, with the random turbulent motion still not sufficiently high to significantly alter bubble trajectories. This is confirmed in the results of Figure 5, where the total number of collisions and coalescences over time (Figure 5(a) and (c)) and the collision efficiency (Figure 5(b) and (d)) are reported. Almost all collisions result in coalescence at both $Re_\tau = 150$ and 590, except in the near-wall region where the largest levels of turbulence are found in the final stages of the transient. Whilst in Figure 5(a) and (c) cumulative values are provided, Figure 5(b) and (d) give the instantaneous coalescence efficiency at $t^+ = 100$ (for $Re_\tau = 150$, Figure 5(b)) and $t^+ = 500$ (for $Re_\tau = 590$, Figure 5(d)). No coalescence efficiency is shown in the lower half of the channel at $Re_\tau = 150$ given the absence of bubbles in that region (Figure 3(a)).

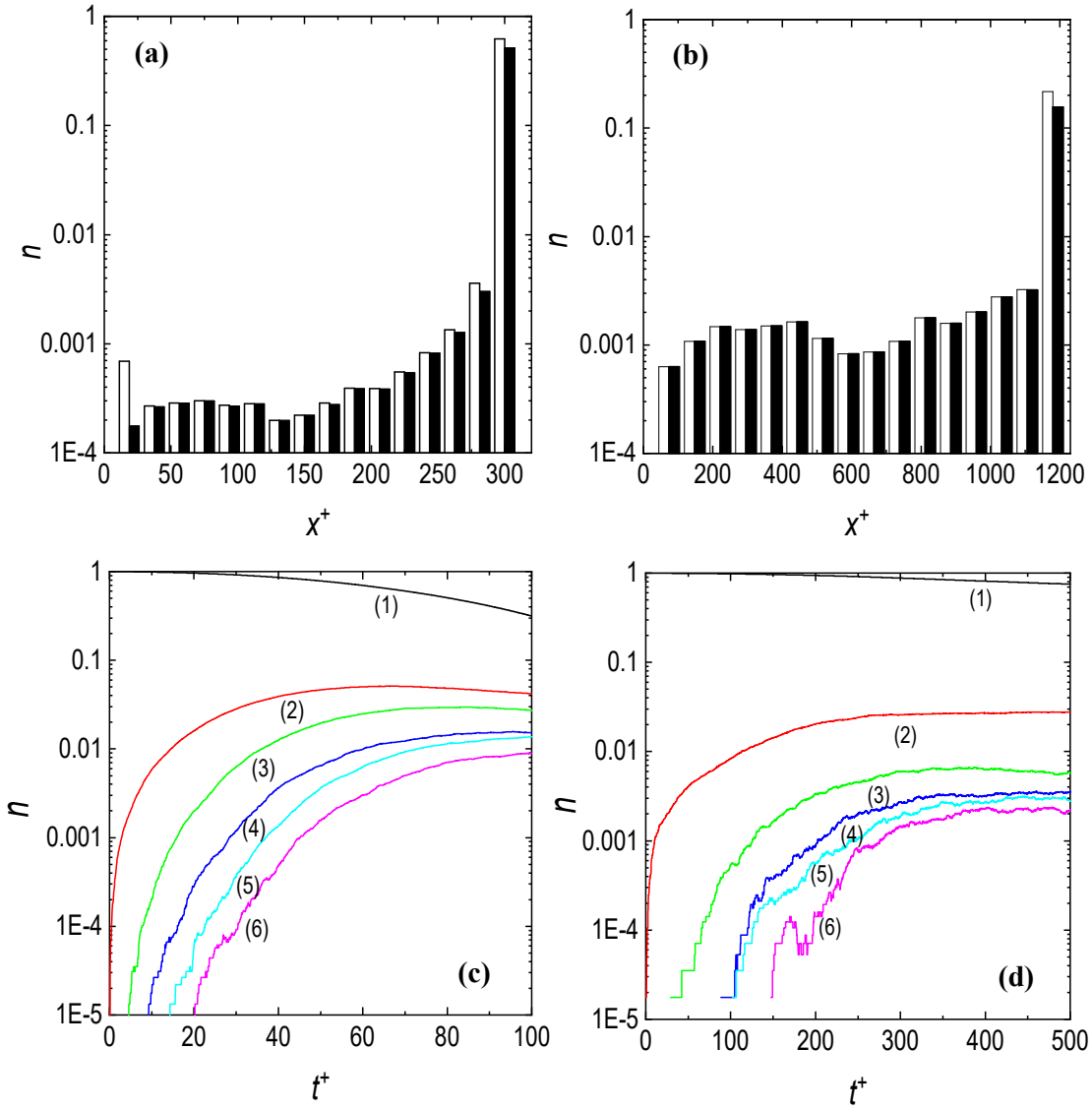

Figure 4. Distribution of bubble collision (□) and coalescence (■) events in the wall-normal direction in the horizontal channel flow at: (a) Re_τ = 150, between t^+ = 0-100; (b) Re_τ = 590, between t^+ = 0-500. Time evolution of the number of bubbles of different sizes (the number in the plots identify the total number of bubbles coalesced) at: (c) Re_τ = 150; (d) Re_τ = 590.

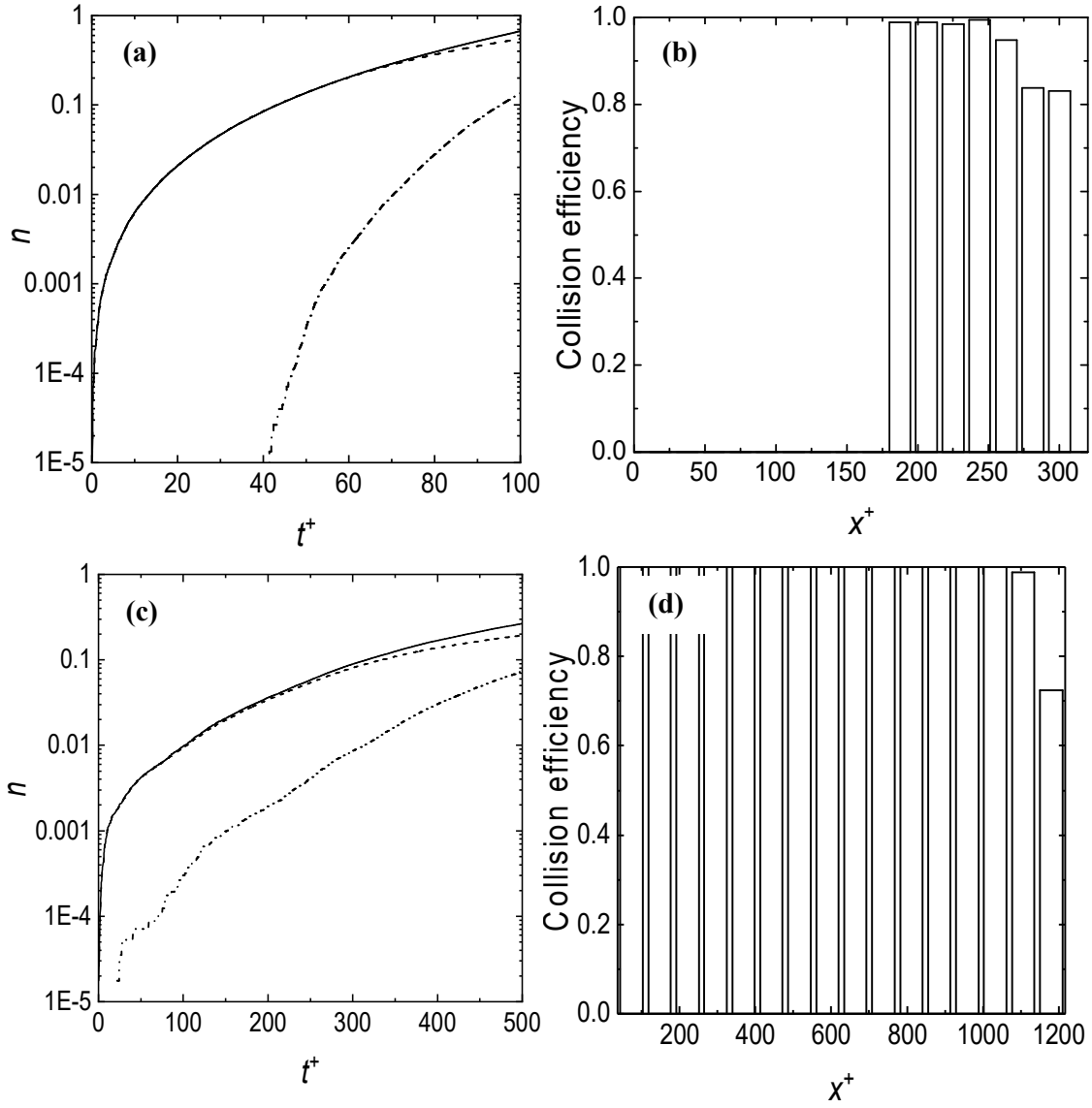

Figure 5. Time evolution of collisions (—), coalescences (---) and collisions without coalescence (···) in the horizontal channel at: (a) Re_τ = 150; (c) Re_τ = 590. Wall-normal distribution of the coalescence efficiency at: (b) Re_τ = 150, at t^+ = 100; (d) Re_τ = 590, at t^+ = 500.

Vertical channel

The four-way coupled model (two-way coupled plus bubble collision, coalescence and breakup) was also applied to a vertical channel with the same geometrical dimensions as the horizontal case. As previously, for this case both single-phase and two-way coupled flows have been considered and validated in an earlier publication[20] to which the interested reader is referred. Starting from fully-developed single-phase solutions at Re_τ = 150 and 590 in both upward and downward flow directions, microbubbles of diameter 110, 220 and 330 μm were

injected into the flows, with the number of bubbles injected varied to give a void fraction of 0.1 % in each flow. Fluid and bubble mean velocities and turbulent stresses are reported in Figure 6 for the Re_τ = 590 and d_b = 220 μm case. Comparable results were obtained in all the other cases. As for the horizontal channel flow, at the void fraction investigated the four-way coupled velocity field is aligned with its single-phase counterpart. Because of buoyancy, the bubbles travel faster than the fluid in upflow, and slower than the fluid in downflow, as shown in Figure 6(c).

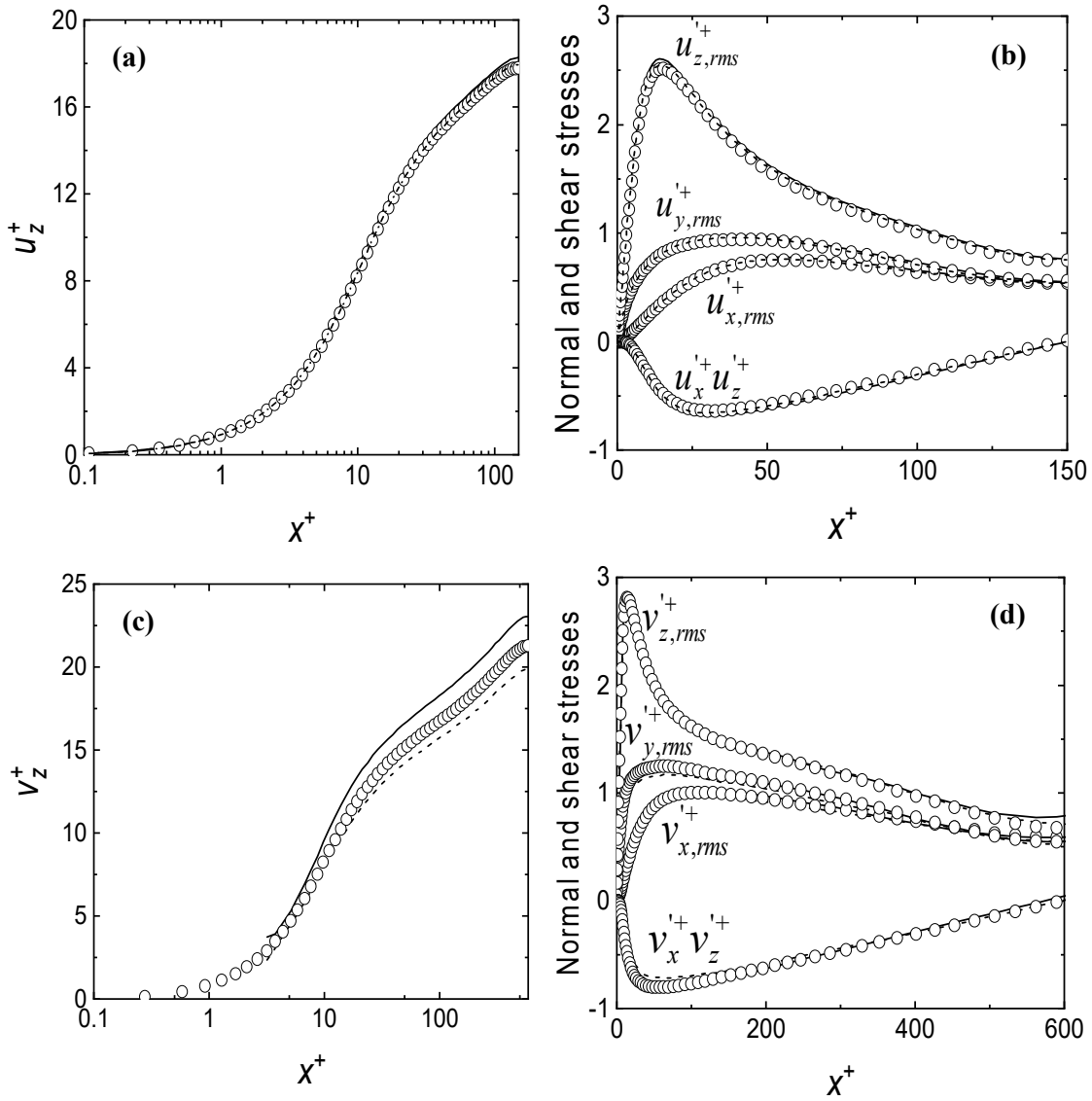

Figure 6. Wall-normal profiles in the vertical channel at Re_τ = 590 with microbubbles of d_b = 220 μm: (a) mean fluid streamwise velocity; (b) fluid normal and shear turbulent stresses; (c)

bubble mean streamwise velocity; (d) bubble normal and shear turbulent stresses. (○ single-phase flow; ─ four-way coupled upward flow; --- four-way coupled downward flow).

Bubble concentration profiles in the vertical channel are shown in Figure 7, averaged over a period of 200 t^+ at Re_τ = 150 and 400 t^+ at Re_τ = 590. Bubble behaviour strongly depends on the flow direction and it is mainly driven by the lift force. In upflow, the bubbles travel faster than the fluid and lift pushes the bubbles towards the wall, and the region of higher relative velocity, because of the asymmetrical liquid flow around the bubbles induced by the liquid shear[49,66]. In contrast, in downflow, where the bubbles are slower than the fluid, the same lift force pushes the bubbles towards the channel centre. Consequently, in upflow, the bubble concentration peaks at the wall, whilst in downflow, a higher, with respect to the upflow case, uniform concentration in the centre of the channel and a bubble-free region near the wall are found. Overall, fluid turbulence enhances bubble random motion and, therefore, favours the movement of bubbles from regions of higher to lower concentration. This is visible in the results of Figure 7 where, contrasting predictions for Re_τ = 150 (Figure 7(a)) and Re_τ = 590 (Figure 7(b)), the wall peak is reduced in upflow and a larger number of bubbles is found in the near-wall bubble depleted region in downflow.

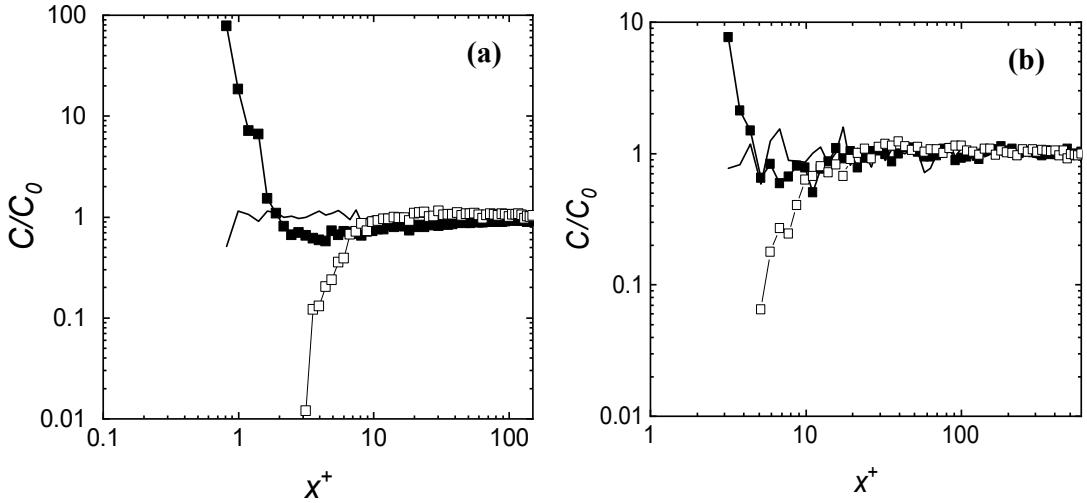

Figure 7. Microbubble normalised wall-normal concentration profiles in the vertical channel flow with microbubbles of d_b = 220 μm at: (a) Re_τ = 150 (─ t^+ = 0; ■ upflow t^+ = 1800 – 2000;

□ downflow $t^+ = 1800 – 2000$); (b) $Re_\tau = 590$ (— $t^+ = 0$; ■ upflow $t^+ = 2200 – 2600$; □ downflow $t^+ = 2200 – 2600$).

In Figure 8, the time evolution of bubble collisions (Figure 8(a) and (c)) and coalescences (Figure 8(b) and (d)) is reported for the upflow and downflow at the two Reynolds numbers considered. The number of collision and coalesce events is normalized by the initial number of bubbles. Overall, the number of collisions and coalescences is higher in upflow than in downflow. This can be related to the slightly higher levels of turbulence in upflow and the very high concentration of bubbles in a narrow region near the wall, which significantly increases collision probability. On the other hand, in downflow, bubbles are uniformly distributed across a larger area in the centre of the channel, and the collision probability decreases accordingly. In all cases, except for the number of collisions in upflow at $Re_\tau = 150$, the number of events increases almost linearly with time, and the large majority of collisions result in coalescence. The superlinear increase in collisions in upflow at $Re_\tau = 150$ (Figure 8(a)) is again due to the high concentration of bubbles near the wall increasing with time which in turn increases the collision probability. Comparing the low (Figure 8(a)) to the high (Figure 8(b)) Reynolds number flows, the lower number of normalised collisions in the latter is due to the comparison being made at the same dimensionless time, which corresponds to a lower physical time at $Re_\tau = 590$ than at 150. Overall, the behaviour with time of the two flows is relatively similar, likely because the increase in collision probability due to greater random turbulent motion is balanced by the reduction in the same probability caused by the lower concentration peak at the wall that such turbulence produces.

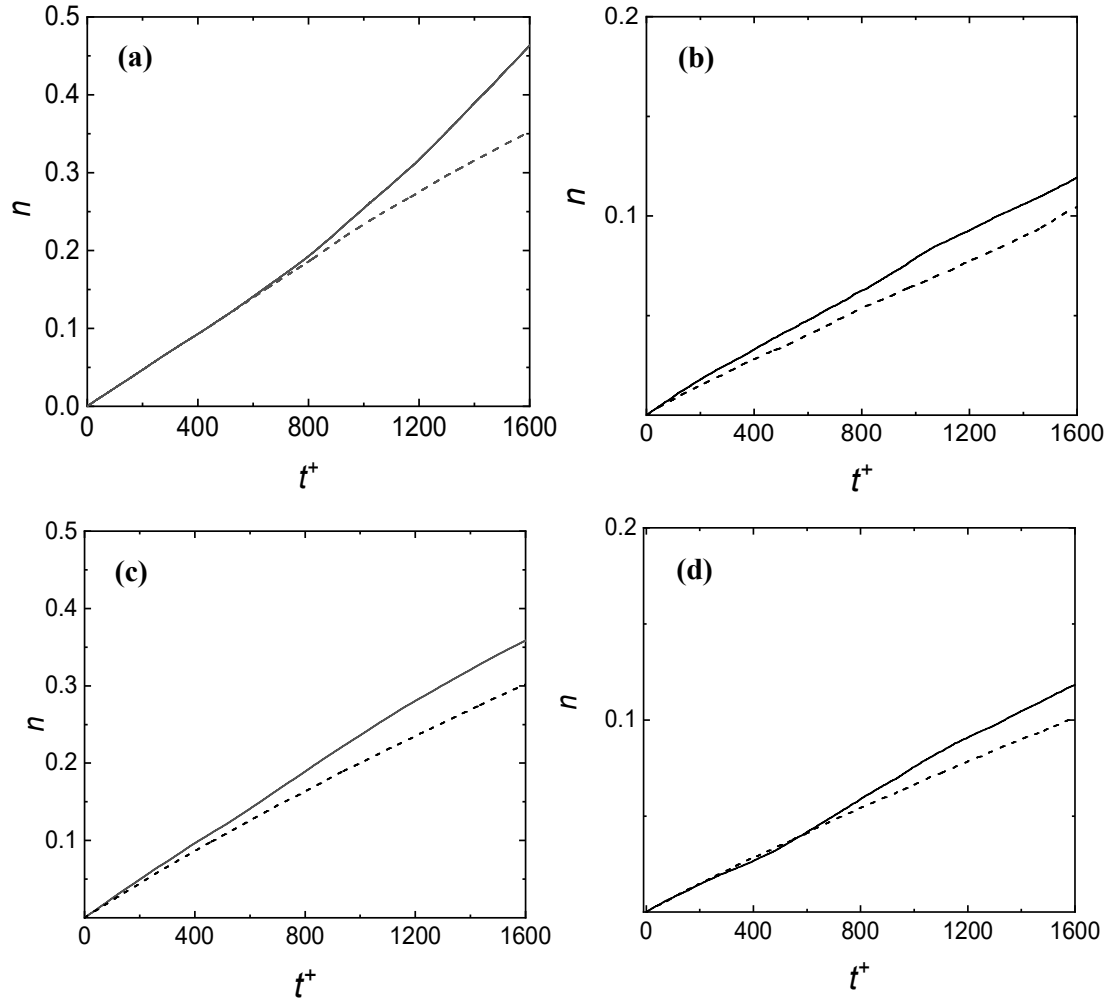

Figure 8. Time evolution of collisions and coalescences in the vertical channel flow with bubbles of d_b = 220 μm: (a) collisions at Re_τ = 150; (b) collisions at Re_τ = 590; (c) coalescences at Re_τ = 150; (d) coalescences at Re_τ = 590 (— upflow; --- downflow).

The spatial distribution of collisions and coalescences in the wall-normal direction is presented in Figure 9 for the three bubble diameters tested, and upward and downward flow conditions. It is immediately clear how almost all collisions result in coalescence, except in the very near-wall regions in upflow for bubbles of diameter 220 μm and 330 μm. The spatial distribution peaks at the two walls in both flows, but this tendency is much more distinct in upflow. Because of the lift force pushing bubbles towards the wall, the higher concentration there favours collision, and coalescence, in those regions. The magnitude of the lift force also increases with the bubble diameter, and the peaks in collisions and coalescences at the wall are more evident

for 220 μm and 330 μm diameter bubbles. Conversely, more uniform distributions are found in downflow, where the lift force pushes bubbles towards the channel centre. The higher turbulence intensities and mean velocity gradients in the near-wall region are still sufficient to induce the greatest number of collisions near the wall, but the difference with those occurring in the channel centre is much less than in upflow, especially for bubbles of 220 μm and 330 μm diameter.

Overall, the number of collisions, normalized by the initial number of bubbles, decreases with increasing bubble diameter in both flows. The void fraction was kept constant in the simulations, therefore fewer bubbles were injected at 220 μm and 330 μm diameter that at 110 μm diameter. In addition to the number of bubbles being reduced, each bubble also has fewer targets to collide with, and the reduction in the number of collisions with decreases in the initial number of bubbles is superlinear.

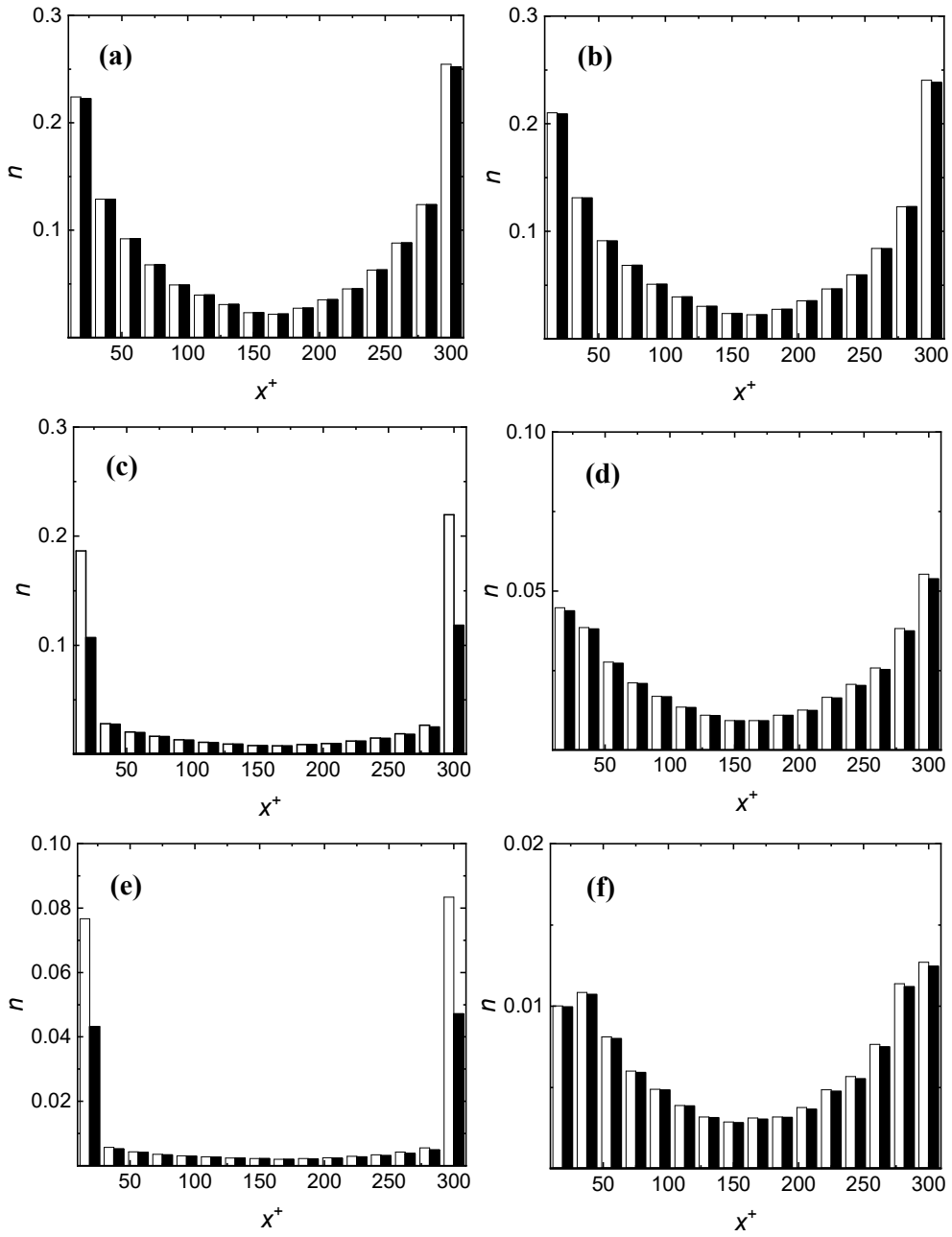

Figure 9. Distribution of bubble collision (□) and coalescence (■) events in the wall-normal direction for the 150 shear Reynolds number vertical upflow ((a), (c) and (e)) and downflow ((b), (d) and (f)): (a-b) d_b = 110 μm; (c-d) d_b = 220 μm; (e-f) d_b = 330 μm.

As already mentioned, the coalescence efficiency differs from almost 100% only near the wall in upflow with bubble diameters of 220 μm and 330 μm. For coalescence to occur, the contact time needs to be higher than the film drainage time, but the latter increases more with the diameter than the former (Eqs. (18) and (19)). This is confirmed by the results of He et al.[67],

who found coalescence was favoured at small bubble diameters. Given that the majority of collisions occur near the wall in upflow, much larger bubbles (a result of multiple coalescence events and characterized by a longer drainage time and reduced coalescence probability) will be generated near the wall. This effect increases with the bubble diameter, because of the higher concentration near the wall and the larger size of the daughter bubbles that are generated by the collision of parent bubbles of initially larger diameter. In addition, the coalescence efficiency close to 100% obtained in both vertical and horizontal channels may be driven by the specific accuracy of the Prince and Blanch model[54]. In previous work[68], this was found to predict an excessive amount of coalescence, although for much larger bubbles having a diameter of a few millimetres. Therefore, further testing will be needed for microbubbles, as well as the assessment of the impact on the prediction of the coalescence efficiency and the bubble diameter of other coalescence models, some more recent, that have been successfully employed in bubbly flows[68-71]. Overall, any detailed validation is challenging, and almost impossible for the coalescence process independently of other parameters. Most of the time, therefore, only the cumulative effect is known through the behaviour of the average bubble diameter, and model accuracy therefore depends on both the models for coalescence and breakup. For microbubbles, in addition, the availability of experimental data is much more limited and some physical aspects of the coalescence process are still not properly understood. Recent studies have also shown contradictory behaviour, with Yonemoto et al.[72] finding a significant amount of coalescence and Park et al.[73], in contrast, observing accumulation of microbubbles in clouds concentrated in low-speed streaks that substantially inhibited coalescence. Although still in need of further clarification, introduction of these local effects in a coalescence model specific to microbubbles is worthy of consideration in future research.

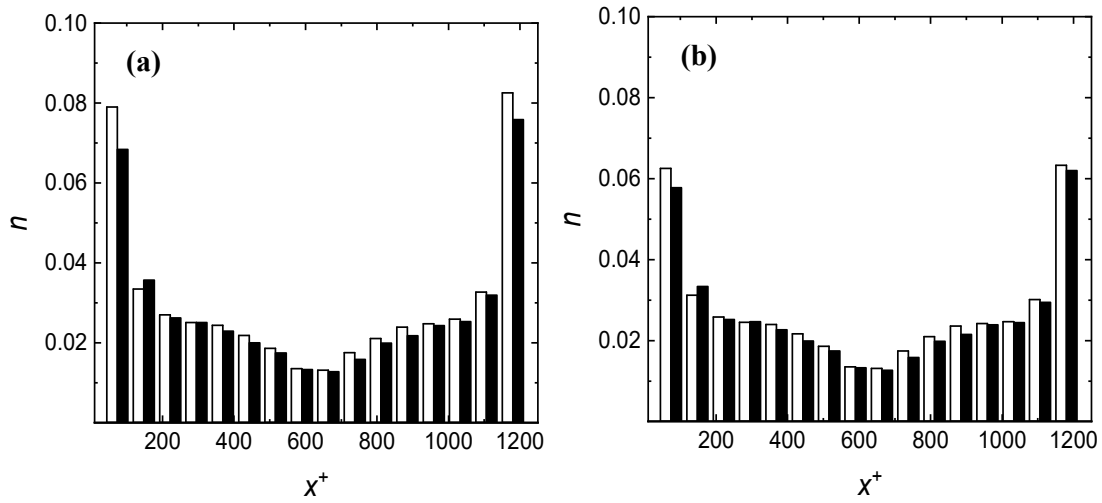

Figure 10. Distribution of bubble collision (□) and coalescence (■) events in the wall-normal direction for the 590 shear Reynolds number vertical flow with microbubbles of diameter d_b = 220 μm: (a) upflow; (b) downflow.

The effect of Reynolds number is addressed in the results given in Figure 10, where the spatial distribution of collisions and coalescences in the wall-normal direction are shown for Re_τ = 590 and bubbles of diameter 220 μm. The collision distribution is more uniform with respect to the same bubble diameter at the lower Reynolds number (Figure 9(c) and (d)), and differences between upflow and downflow are less evident. This is directly related to the random mixing promoted by turbulence and the more uniform bubble concentration profile across the channel. The birth of large bubbles in the near-wall region from multiple coalescences, which are less prone to further coalescence, is also limited and the coalescence efficiency in upflow (Figure 10(a)) is higher than in Figure 9(c) at lower Re_τ. In downflow, the distribution shows a higher peak at the wall with respect to that in the Re_τ = 150 flow in Figure 9(d). This is again due to the additional mixing promoted by turbulence that limits the migration of bubbles towards the channel centre and away from the regions of highest turbulence near the wall. Overall, the increase in turbulence tends to compete with, and partially override, the distinctive effect of flow orientation on bubble behaviour.

Bubble breakup

Normally, the bubble size distribution is modified not only through coalescence but also following the breakup of bubbles induced by velocity gradients or turbulent velocity fluctuations. Restoring forces driven by the surface tension, however, are inversely proportional to the bubble radius and, for the flow conditions studied so far, sufficient to compensate any stress induced on the surface of the microbubbles. No bubble breakup was therefore observed for the cases considered above. Therefore, to test the full capabilities of the model with breakup and coalescence, the flow of refrigerant R134a was also simulated at Re_τ = 1154. The higher flow Reynolds number, and the lower surface tension of R134a vapour bubbles, allowed a sufficient number of breakups to be recorded in the flow for meaningful statistics to be generated. The breakup evolution for two bubble diameters, 110 μm and 220 μm, are shown in Figure 11 for upward and downward flow conditions. The number of breakups is much smaller when compared to coalescences, even with the lower surface tension and the higher turbulence intensity. The number of breakups increases with the bubble diameter since the surface restoring force is inversely proportional to, and the turbulence induced stresses directly proportional to, the bubble diameter. Figure 11(c) and (d) show clearly that the small number of breakups occur in the region of highest turbulence near the wall.

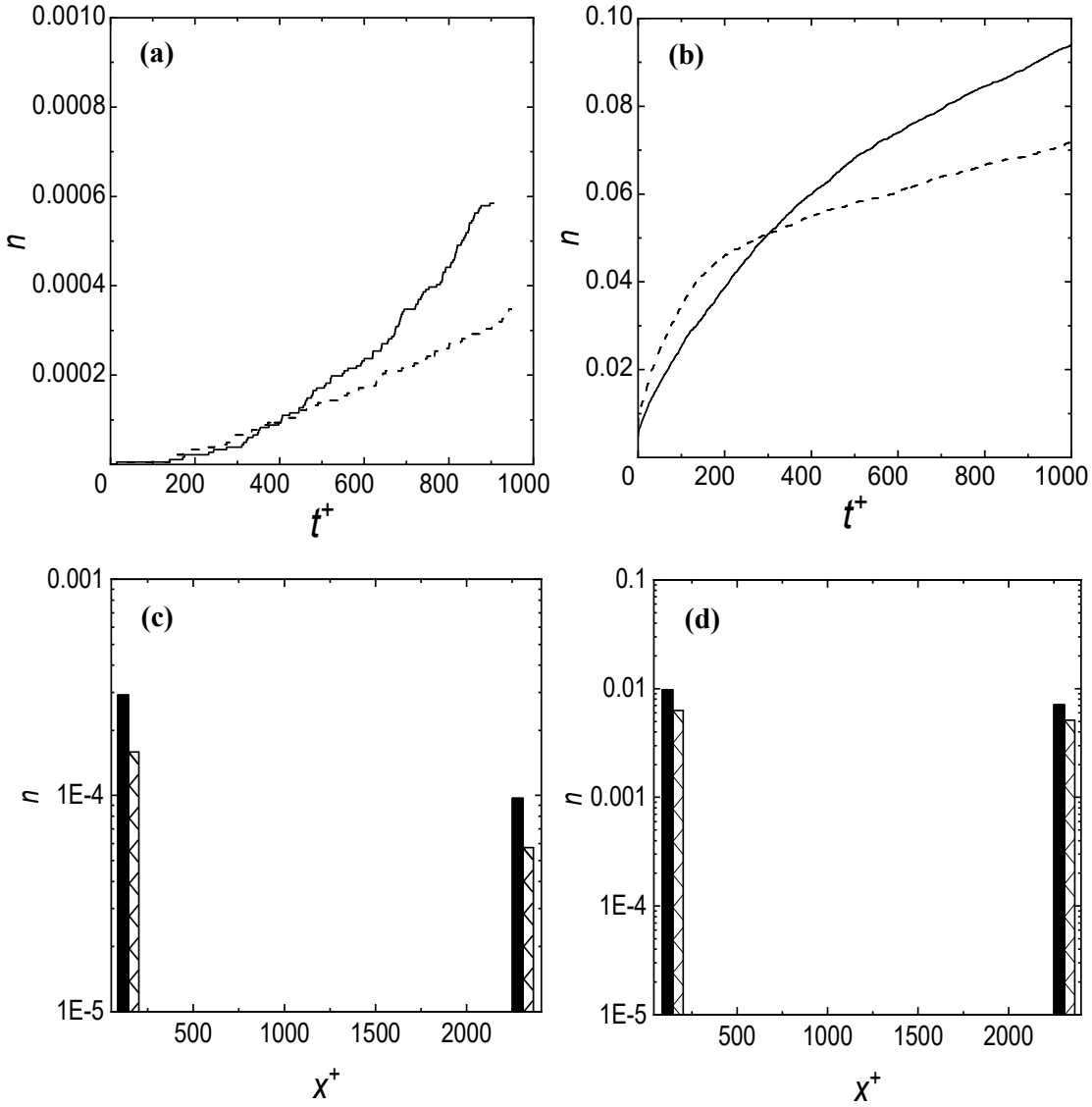

Figure 11. Time evolution of the total number of breakup events in the R134a flow at Re_τ = 1154: (a) d_b = 110 μm; (b) d_b = 220 μm (— upflow; --- downflow). Distribution of bubble breakup in the wall-normal direction: (c) d_b = 110 μm; d_b = 220 μm; (■ upflow; □ downflow).

The full capabilities of the present model are displayed in the results of Figure 12, where breakup and coalescence are both enabled for the R134a flow at Re_τ = 1154. Coalescence patterns do not show any significant differences with what has been observed for the flows considered in the previous sections, although the higher turbulence intensity makes the coalescence distribution even more homogeneous across the channel, almost overcoming lift force and bubble diameter effects. The number of breakups is much smaller compared to the

coalescences, in particular at 110 μm, and the breakups remain confined to the near-wall region. Therefore, coalescence is still dominant. Nevertheless, these results demonstrate the model's ability to predict both coalescence and breakup events, and their mutual interaction, and the way in which such events determine the evolution of the bubble diameter distribution in such flows.

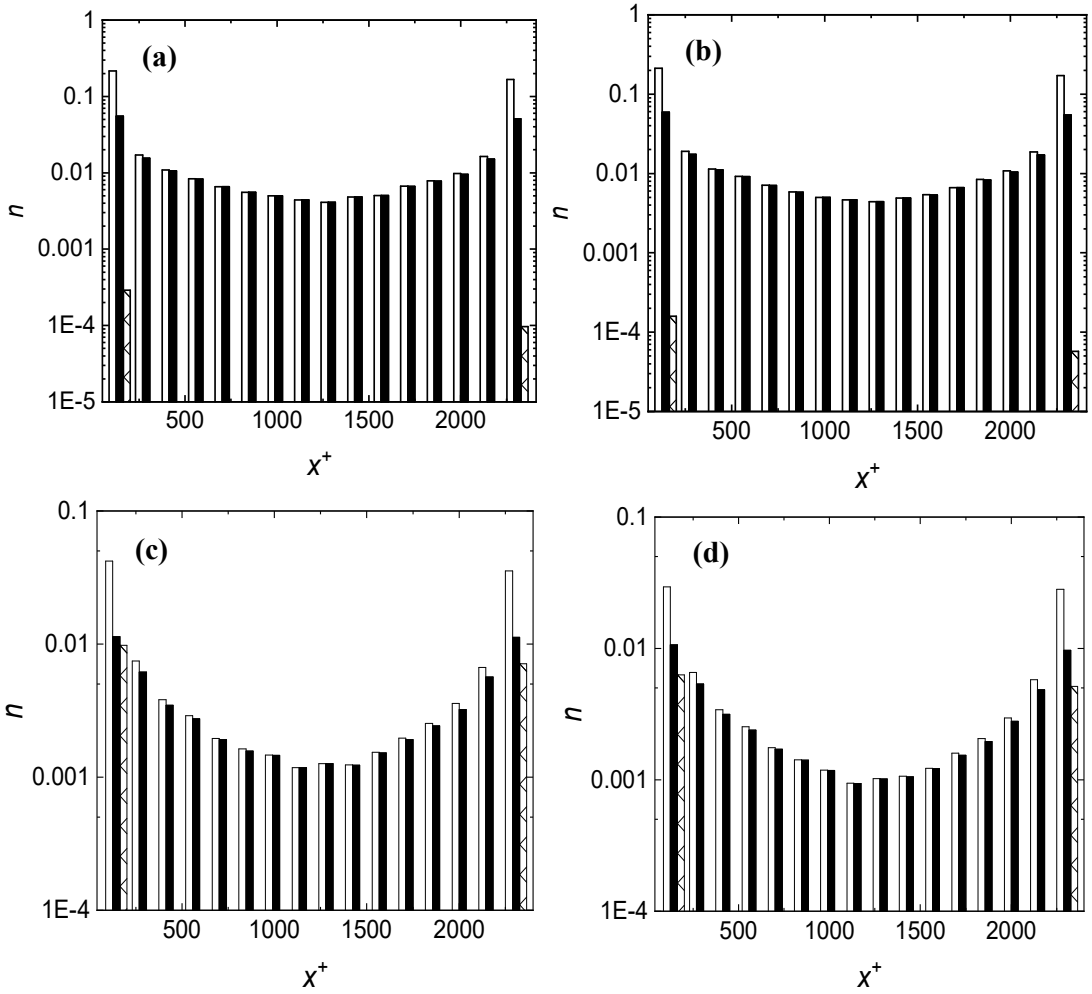

Figure 12. Distribution of bubble collision (□), coalescence (■) and breakup (⊟) events in the wall-normal direction for the R134a flow at $Re_\tau = 1154$: (a) upflow, $d_b = 110$ μm; (b) downflow, $d_b = 110$ μm; (c) upflow, $d_b = 220$ μm; (d) downflow, $d_b = 220$ μm.

Conclusions

Four-way coupled simulations (two-way coupled plus bubble collision, coalescence and breakup) of two-phase microbubble-laden channel flows were undertaken using an Eulerian-

Lagrangian technique with large eddy simulation employed to predict the turbulent continuous liquid flow and Lagrangian tracking to compute bubble trajectories. The model is fully capable of predicting bubble coalescence and breakup, and was applied to computing horizontal, and vertical upward and downward, channel flows.

Simulation results provided insights into bubble behaviour and information on the occurrence and distribution of bubble collisions and coalescences. By driving the bubble distribution, gravity in the horizontal flow, and the lift force in the vertical channel, mostly determined collision patterns at low Reynolds numbers. Most of the collisions occur near the wall in the horizontal and the vertical upward channel, while the distribution is much more uniform in vertical downflow, where bubbles are more uniformly distributed in a large region in the centre of the channel. The higher probability of collision in the region dense with bubbles near the wall drives the number of collisions higher in upflow than in downflow. This preferential distribution of collisions increases with the bubble diameter, because of the stronger lift force.

The coalescence efficiency was almost always 100%, except in the near-wall region in vertical upward flow with 220 μm and 330 μm diameter bubbles, likely because of the formation in these cases of larger bubbles that are less prone to coalescence. Overall, and although the accuracy of the employed Prince and Blanch[54] coalescence model with respect to other available formulations will need to be further tested, this result suggests that the bubbles collide with low relative velocities and have long contact times, and that the fluid turbulent motion has a limited impact on single bubble trajectories at the shear Reynolds numbers investigated. However, turbulence levels were high enough to oppose preferential concentration and counteract the effects of gravity and the lift force on collision distributions, resulting in more uniform distributions at a shear Reynolds number of 590 in all configurations. In the latter

flows, the increase in collisions driven by the higher levels of turbulence was balanced by a reduction in the regions where preferential concentration occurred, resulting in a similar total numbers of events for the two Reynolds numbers considered.

Even at a shear Reynolds number of 590, turbulence was not sufficient to breakup air bubbles, and additional simulations were made with refrigerant R134a at $Re_\tau = 1154$. Even in this case, coalescence remains dominant and breakup is constrained to regions of high turbulence near the wall.

Overall, the results presented demonstrate the successful implementation of coalescence and breakup routines in the overall model, and its ability of providing insight into bubble behaviour and bubble size evolution in turbulent flows. Additionally, the results presented are of value in support of the development of more macroscopic predictive methodologies such as those employed in Eulerian-Eulerian multi-fluid models. At the present time, one of the major limitations in the work described is the lack of relevant experimental data which has precluded any detailed quantitative validation of the overall model. In future studies, other than further improving the model in the areas that have been identified, such as the drag and the coalescence models, a thorough validation of the model will be pursued whenever made possible by experimental measurements that become available.

References

1. Ishii M, Hibiki T. *Thermo-fluid dynamics of two-phase flow*. New York, USA: Springer; 2006.
2. Lehr F, Millies M, Mewes D. Bubble-size distributions and flow fields in bubble columns. *AIChE J.* 2002;48:2426-2443.
3. Risso F. Agitation, mixing and transfers induced by bubbles. *Annu Rev Fluid Mech.* 2018;50:25-48.
4. Feng J, Bolotnov IA. Evaluation of bubble-induced turbulence using direct numerical simulation. *Int J Multiphase Flow.* 2017;93:92-107.
5. Liu TJ, Bankoff SG. Structure of air-water bubbly flow in a vertical pipe - I. Liquid mean velocity and turbulence measurements. *Int J Heat Mass Tran.* 1993;36:1049-1060.

6. Liu TJ, Bankoff SG. Structure of air-water bubbly flow in a vertical pipe - II. Void fraction, bubble velocity and bubble size distribution. *Int J Heat Mass Tran.* 1993;36:1061-1072.
7. Colombo M, Fairweather M. RANS simulation of bubble coalescence and break-up in bubbly two-phase flows. *Chem Eng Sci.* 2016;146:207-225.
8. Liu H, Hibiki T. Bubble breakup and coalescence models for bubbly flow simulation using interfacial area transport equation. *Int J Heat Mass Tran.* 2018;126:128-146.
9. Liao Y, Lucas D. A literature review of theoretical models for drop and bubble breakup in turbulent dispersions. *Chem Eng Sci.* 2009;64:3389-3406.
10. Liao Y, Lucas D. A literature review on mechanisms and models for the coalescence process of fluid particles. *Chem Eng Sci.* 2010;65:2851-2864.
11. Colombo M, Fairweather M. Multiphase turbulence in bubbly flows: RANS simulations. *Int J Multiphase Flow.* 2015;77:222-243.
12. Colombo M, Fairweather M. Influence of multiphase turbulence modelling on interfacial momentum transfer in two-fluid Eulerian-Eulerian CFD models of bubbly flows. *Chem Eng Sci.* 2019;195:968-984.
13. Hosokawa S, Hayashi K, Tomiyama A. Void distribution and bubble motion in bubbly flows in a 4 x 4 rod bundle. Part I: Experiments. *J Nucl Sci Technol.* 2014;51:220-230.
14. Hosokawa S, Tomiyama A. Multi-fluid simulation of turbulent bubbly pipe flow. *Chem Eng Sci.* 2009;64:5308-5318.
15. Liao Y, Ma T, Liu L, Ziegenhein T, Krepper E, Lucas D. Eulerian modelling of turbulent bubbly flow based on a baseline closure concept. *Nucl Eng Des.* 2018;337:450-459.
16. Lubchenko N, Magolan B, Sugrue R, Baglietto E. A more fundamental wall lubrication force from turbulent dispersion regularization for multiphase CFD applications. *Int J Multiphase Flow.* 2018;98:36-44.
17. Lucas D, Beyer M, Szalinski L, Schutz P. A new databse on the evolution of air-water flows along a large vertical pipe. *Int J Therm Sci.* 2010;49:664-674.
18. Rzehak R, Krepper E, Liao Y, Ziegenhein T, Kriebitzsch P, Lucas D. Baseline model for the simulation of bubbly flows. *Chem Eng Technol.* 2015;38:1972-1978.
19. Yao W, Morel C. Volumetric interfacial area prediction in upward bubbly two-phase flow. *Int J Heat Mass Tran.* 2004;47:307-328.
20. Asiagbe KS, Fairweather M, Njobuenwu DO, Colombo M. Large eddy simulation of microbubble dispersion and flow field modulation in vertical channel flows. *AIChE J.* 2019;65:1325-1339.
21. Giusti A, Lucci F, Soldati A. Influence of the lift force in direct numerical simulation of upward/downward turbulent channel flow laden with surfactant contaminated microbubbles. *Chem Eng Sci.* 2005;60(22):6176-6187.
22. Molin D, Marchioli C, Soldati A. Turbulence modulation and microbubble dynamics in vertical channel flow. *Int J Multiphase Flow.* 2012;42(0):80-95.
23. Pang M, Wei J, Yu B. Investigation on influences of bubble location and momentum transfer direction on liquid turbulence modification for the dilute bubbly flow. *Int J Fluid Mech Res.* 2016;43(2):161-181.
24. Chertok B, Langer R. Circulating magnetic microbubbles for localized real-time control of drug delivery by ultrasonography-guided magnetic targeting and ultrasound. *Theranostics.* 2018;8:341-357.
25. Wischhusen J, Padilla F. Ultrasound-tartgeted microbubble destruction (UTMD) for localized drug delivery into tumor tissue. *IRBM.* 2018;40:10-15.
26. Liu Y, Shen X, Sun J, Li P, Zhang A. Treatment of aniline contaminated water by a self-designed dielectric barrier discharge reactor coupling with micro-bubbles: optimization of the system and effects of water matrix. *J Chem Technol Biot.* 2019;94:494-504.

27. Zhang J, Huang GQ, Liu C, Zhang RN, Chen XX, Zhang L. Synergistic effect of microbubbles and activated carbon on the ozonation treatment of synthetic dyeing wastewater. *Sep Purif Technol.* 2018;201:10-18.
28. Song W, Wang C, Wei Y, Zhang X, Wang W. Experimental study of microbubble drag reduction on an axisymmetric body. *Mod Phys Lett B.* 2018;32:1850035.
29. Rzehak R, Ziegenhein T, Kriebitzsch P, Krepper E, Lucas D. Unified modelling of bubbly flows in pipes, bubble columns, and airlift columns. *Chem Eng Sci.* 2017;157:147-158.
30. Dabiri S, Tryggvason G. Heat transfer in turbulent bubbly flow in vertical channel. *Chem Eng Sci.* 2015;122:106-113.
31. Mehrabani MT, Nobari MRH, Tryggvason G. An efficient front-tracking method for simulation of multi-density bubbles. *Int J Numer Meth Fl.* 2017;84:445-465.
32. Santarelli C, Fröhlich J. Direct Numerical Simulations of spherical bubbles in vertical turbulent channel flow. Influence of bubble size and bidispersity. *Int J Multiphase Flow.* 2016;81:27-45.
33. Pang M, Wei JJ, Yu B. Numerical study on modulation of microbubbles on turbulence frictional drag in a horizontal channel. *Ocean Eng.* 2014;81:58-68.
34. Lau YM, Bai W, Deen NG, Kuipers JAM. Numerical study of bubble break-up in bubbly flows using a deterministic Euler–Lagrange framework. *Chem Eng Sci.* 2014;108:9-22.
35. Masterov MV, Baltussen MW, Kuipers JAM. Numerical simulation of a square bubble column using Detached Eddy Simulation and Euler–Lagrange approach. *Int J Multiphase Flow.* 2018;107:275-288.
36. Asiagbe KS, Fairweather M, Njobuenwu DO, Colombo M. Large eddy simulation of microbubble transport in a turbulent horizontal channel flow. *Int J Multiphase Flow.* 2017;94:80-93.
37. Ma T, Santarelli C, Ziegenhein T, Lucas D, Frohlich J. Direct numerical simulation-based Reynolds-averaged closure for bubble-induced turbulence. *Phys Rev Fluids.* 2017;2:034301.
38. Magolan B, Baglietto E, Brown C, Bolotnov IA, Tryggvason G, Lu J. Multiphase turbulence mechanisms identification from consistent analysis of direct numerical simulation data. *Nucl Eng Technol.* 2017;49:1318-1325.
39. Germano M, Piomelli U, Moin P, Cabot WH. A dynamic subgrid-scale eddy viscosity model. *Phys Fluids.* 1991;3(7):1760-1765.
40. Piomelli U, Liu J. Large-Eddy simulation of rotating channel flows using a localized dynamic model. *Phys Fluids.* 1995;7:839-848.
41. di Mare L, Jones WP. LES of turbulent flow past a swept fence. *Int J Heat Fluid Fl.* 2003;24(4):606-615.
42. Lilly DK. The representation of small scale turbulence in numerical simulation experiments. *Proceedings of the IBM Scientific Computing Symposium on Environmental Sciences*. Yorktown Heights, USA: H. H. Goldstine IBM; 1967:195-210.
43. Maxey MR, Riley JJ. Equation of motion for a small rigid sphere in a nonuniform flow. *Phys Fluids.* 1983;26(4):883-889.
44. Rivero M, Magnaudet J, Fabre J. New results on the forces exerted on a spherical body by an accelerated flow. *C.R. Acad Sci Paris Serie II.* 1991;312:1499-1506.
45. Sridhar G, Katz J. Effect of entrained bubbles on the structure of vortex rings. *J Fluid Mech.* 1999;397:171-202.
46. Schiller L, Naumann Z. A drag coefficient correlation. *Z Ver Deutsch Ing.* 1935;77:318-320.
47. Ishii M, Zuber N. Drag coefficient and relative velocity in bubbly, droplet or particulate flows. *AIChE J.* 1979;25:843-855.

48. Tomiyama A, Kataoka I, Zun I, Sakaguchi T. Drag coefficients of single bubbles under normal and micro gravity conditions. *JSME International Journal Series B Fluids and Thermal Engineering.* 1998;41:472-479.
49. Legendre D, Magnaudet J. A note on the lift force on a spherical bubble or drop in a low-Reynolds-number shear flow. *Phys Fluids.* 1997;9(11):3572-3574.
50. Bini M, Jones WP. Large-eddy simulation of particle-laden turbulent flows. *J Fluid Mech.* Nov 2008;614:207-252.
51. Hoomans BPB, Kuipers JAM, Briels WJ, van Swaaij WPM. Discrete particle simulation of bubble and slug formation in a two-dimensional gas fluidised bed: a hard-sphere approach. *Chem Eng Sci.* 1996;51:99-118.
52. Vreman B, Geurts BJ, Deen NG, Kuipers JAM, Kuerten JGM. Two- and four-way coupled euler-lagrangian large-eddy simulation of turbulent particle-laden channel flow. *Flow Turbul Combust.* 2009;82:47-71.
53. Breuer M, Alletto M. Efficient simulation of particle-laden turbulent flows with high mass loadings using LES. *Int J Heat Fluid Fl.* 2012;35:2-12.
54. Prince MJ, Blanch HW. Bubble coalescence and breakup in air-sparged bubble columns. *AIChE J.* 1990;36:1485-1499.
55. Sommerfeld M, Bourloutski E, Broder D. Euler/Lagrange calculations of bubbly flows with consideration of bubble coalescence. *Can J Chem Eng.* 2003;81:508-518.
56. Martinez-Bazan C, Montanes JL, Lasheras JC. On the breakup of an air bubble injected into a fully developed turbulent flow. Part 1. Breakup frequency. *J Fluid Mech.* 1999;401:157-182.
57. Gamet L, Ducros F, Nicoud F, Poinsot T. Compact finite difference schemes on non-uniform meshes. Application to direct numerical simulations of compressible flows. *Int J Numer Meth Fl.* 1999;29(2):159-191.
58. Gear CW. *Numerical initial value problems in ordinary differential equations*. Englewood Cliffs, NJ, USA: Prentice-Hall; 1973.
59. Patankar SV, Spalding DB. A calculation procedure for heat, mass and momentum transfer in three-dimensional parabolic flows. *Int J Heat Mass Tran.* 1972;15:1787.
60. Rhie CM, Chow WL. Numerical study of the turbulent flow past an airfoil with trailing edge separation. *AIAA J.* 1983;31:1525-1533.
61. Van der Vorst HA. BI-CGSTAB a fast and smoothly converging variant of BI-CG for the solution of non-symmetric linear systems. *SIAM J Sci Stat Comput.* 1992;13:631-644.
62. Kershaw DS. The incomplete Cholesky-conjugate gradient method for the iterative solution of systems of linear equations. *J Comput Phys.* 1978;26:43-65.
63. di Mare F, Jones WP, Menzies KR. Large eddy simulation of a model gas turbine combustor. *Combust Flame.* 2004;137(3):278-294.
64. Jones WP, Marquis AJ, Vogiatzaki K. Large-eddy simulation of spray combustion in a gas turbine combustor. *Combust Flame.* 2014;161(1):222-239.
65. Njobuenwu DO, Fairweather M. Dynamics of single, non-spherical ellipsoidal particles in a turbulent channel flow. *Chem Eng Sci.* 2015;123(0):265-282.
66. Rzehak R, Krepper E. CFD modeling of bubble-induced turbulence. *Int J Multiphase Flow.* 2013;55:138-155.
67. He C, Bi XT, Grace JR. Monitoring electrostatics and hydrodynamics in gas–solid bubbling fluidized beds using novel electrostatic probes. *Ind Eng Chem Res.* 2015;54:8333-8343.
68. Liao Y, Rzehak R, Lucas D, Krepper E. Baseline closure model for dispersed bubbly flow: Bubble coalescence and breakup. *Chem Eng Sci.* 2015;122:336-349.
69. Mitre JF, Takahashi RSM, Ribeiro CP, Lage PLC. Analysis of breakage and coalescence models for bubble columns. *Chem Eng Sci.* 2010;65:6089-6100.

70. Mukin R. Modeling of bubble coalescence and break-up in turbulent bubbly flow. *Int J Multiphase Flow.* 2014;62:52-66.
71. Wang T. Simulation of bubble column reactors using CFD coupled with a population balance model. *Front Chem Sci Eng.* 2011;5(162-172).
72. Yonemoto Y, Yanagisawa H, Kawara Z, Kunugi T. Coalescence of microbubble. *J JSEM.* 2008;8:38-44.
73. Park HJ, Saito D, Tasaka Y, Murai Y. Color-coded visualization of microbubble clouds interacting with eddies in a spatially developing turbulent boundary layer. *Exp Therm Fluid Sci.* 2019(109):109919.